

Article

Characterization of Tensile Crack Propagation and Energy Evolution during the Failure of Coal–Rock Samples Containing Holes

Chen Jing¹ and Lei Zhang^{2,*} ¹ Ventilation Department, Shaanxi Shanmei Huangling Mining (Group) Co., Ltd., Yan'an 727300, China² College of Energy Engineering, Xi'an University of Science and Technology, Xi'an 710054, China

* Correspondence: zhang.lei@xust.edu.cn

Abstract: The instability and fracturing of gas drainage boreholes are one of the main causes of low drainage efficiency. Based on the rock mass energy principle and the Barenblatt model, the energy evolution of the coal–rock mass around the hole, the conversion characteristics of the dissipated energy U^d , and the propagation pattern of the initial tensile cracks were investigated. The results show that based on the conversion process of the dissipated energy, the failure process of samples containing holes can be divided into an initial dissipation stage, a decelerated dissipation stage, a stable dissipation stage, and an accelerated dissipation stage. The dissipated energy is always greater than the elastic energy during the first half of loading, and it is mainly used for the continuous development and propagation of initial tensile cracks. Then, remote cracks and cracks to the left and right of the hole boundary are generated to inhibit the propagation of the tensile cracks. Later, when the energy storage limit is reached, the elastic strain energy around the hole is released, and the macroscopic failure cracks propagate and coalesce, which causes the stress environment to change and the tensile cracks to reopen and finally propagate. The tensile cracks in the upper and lower ends of the holes undergo an opening–closing–reopening process, and the presence of cohesion $c(x)$ hinders the propagation of the tensile cracks that are formed by the generation and migration of fracture initiation zone, friction zone, and intact zone. The dissipated energy released was related to the different stages of the tensile crack propagation, which could be used for the structure monitoring and flaw predicting of the gas drainage borehole.

Keywords: Barenblatt cohesion model; gas drainage boreholes; crack propagation; hole-containing specimen; crack inhibition; tensile cracks; strain energy; dissipated energy



Citation: Jing, C.; Zhang, L. Characterization of Tensile Crack Propagation and Energy Evolution during the Failure of Coal–Rock Samples Containing Holes. *Sustainability* **2022**, *14*, 14279. <https://doi.org/10.3390/su142114279>

Academic Editor: Haiyan Wang

Received: 27 September 2022

Accepted: 26 October 2022

Published: 1 November 2022

Publisher's Note: MDPI stays neutral with regard to jurisdictional claims in published maps and institutional affiliations.



Copyright: © 2022 by the authors. Licensee MDPI, Basel, Switzerland. This article is an open access article distributed under the terms and conditions of the Creative Commons Attribution (CC BY) license (<https://creativecommons.org/licenses/by/4.0/>).

1. Introduction

The stability of drainage holes ensures that the gas drainage rate meets the standard. Under external loading, new cracks are generated in the coal–rock mass around the hole. Then, these cracks develop, propagate, and coalesce with the remote original cracks, causing problems such as borehole cracking, delamination, and collapse and resulting in borehole failure. Therefore, it is of great significance to study the fracture pattern of samples containing holes under stress to reveal the deformation and failure of drainage holes.

In the early stage, the image of crack propagation was used for evaluating the damage to the hole structure [1–3]. What makes researchers more interested is the behavior of the crack. Thus, a finite-width crack model and the fourth-order phase-field model combining the non-standard phase-field form with a cohesive zone model were presented to illustrate the crack propagation [3,4]. The Barenblatt cohesion model was used to study the inhibition of the propagation of the tensile cracks by stress [5,6]. A numerical approach based on the meshfree methods and an algorithm combined based on the anisotropic damage plasticity model were developed for calculating the beginning of a crack and predicting the fatigue

crack growth path [7–9]. Even the classical fails could be predicted by the scale-invariant cohesive crack model [10]. However, there is bias in predicting the crack which was confirmed as the size effect later [11]. To cover these drawbacks, scale-independent cohesive law and a single cohesive curve approach were presented [12,13]. The related works showed that the energetic and statistical-energetic theories can predict the dependence of size effect law parameters on the structure geometry [11,14]. As the external energy drive is the essence of instability and failure inside a material, even the external energy such as explosive detonation and plasma subject to the rock can cause some breaking [15,16]. Many scholars have studied the energy evolution of coal and rock masses to address the characteristics during the destruction. Based on energy analysis, the energy dissipation and release of a rock mass were systematically elaborated to establish a rock failure criterion [17–19]. Various parameters related to the energy were used for establishing the relationship between the rock deformation and energy conversion, such as the energy iterative growth factor [20], energy dissipation ratio [20,21], energy loss [22], minimum energy principle for the dynamic failure [23], energy number [24–26], energy release rate [27], and amplitude of the energy fluctuations [28–30]. Moreover, there are methodologies based on strain energy density [31], the extended maximum tangential strain criterion [32], the mixed-mode brittle fracture criterion [33], the phase-field model [34], and a higher-order micromechanics-based approach [3,35], which were presented to predict crack growth.

However, this was not the case when facing the problem with gas drainage boreholes. The instability failure of boreholes had three categories, which were stress-controlled failure, structural plane-controlled failure, and gas blowout from soft coal seams [36]. According to the experiment, the cracks around the hole were divided into remote, primary, and shear, according to their location distribution and stress characteristics [2,37,38]. These cracks' interaction contributed to the damage to the rock causing destruction [39]. The results of many experiments and numerical calculations verified the three types of cracks [40–42]. The stress distribution around the different types of cracks was also reconstructed by the surface stress inversion [43]. That means the energy evolution would have some differences concerning the crack types, which coincide with the electric potential experiment [44]. Numerous studies have been performed on the energy evolution and fracture characteristics of rock samples, but these studies only determined the corresponding relationship between the energy change process and the fracture morphology. Few studies have been conducted on the influence of the energy flow on crack development, and the energy evolution of samples containing holes has rarely been reported. However, the crack around the gas drainage boreholes seriously affects extraction efficiency, as monitoring and detecting the status of boreholes becomes the daily work of coal mines. The investigation of the initial tensile crack propagation pattern and the corresponding mechanism is crucial to the failure analysis of gas drainage boreholes, as it is the early symptom and reason why the gas drainage fails.

Therefore, for a better understanding of the propagation of the tensile crack around the gas drainage boreholes and to provide monitoring and detecting theory as well as method, the observation of the failure process of coal–rock samples containing holes was conducted. As the crack propagation and the slip between fissures with energy changes, the energy principle gives a perspective to investigate the failure of the hole structure such as the gas drainage borehole. As well as the cohesion model being introduced, the Barenblatt model delicately avoids the singularity of the crack tip in elastic mechanics. Thus, the rock mass energy principle and the Barenblatt model were used to investigate the energy evolution characteristics of the coal–rock mass around the hole in the study. A model for crack propagation in samples under energy control was established, which can provide a better understanding of the gas drainage borehole destruction. With these energy evolution characteristics and the digital image correlation, the monitoring technology of boreholes becomes available, and this article will provide some references for this technology.

2. Materials and Methods

2.1. Sample Preparation

To simulate the gas drainage structure and materials as closely as possible, the selection and proportioning of raw materials is an important part of the experiment [45,46]. In the experiment conducted in this study, the slurry was prepared using a mixture of gypsum and water with a mass ratio of 7:3 [2,42]. The gas drainage borehole is in the pre-peak and post-peak stages of a coal seam, which correspond to the failure process of a sample from initial loading to the crackdown. Though the size effect influences the uniaxial compressive strength (UCS), it does not change the characteristics and pattern of the sample. In addition, the structure of the hole plays a significant role in the test [47–49]. Thus, the bias induced by the size effect has little effect on the experiment result. Here, the diameter of the gas drainage borehole was scaled to be 1/10, as the diameter of the commonly used borehole in the coal mine is about 100 mm. In addition, the end effect should take into consideration that the required length of the end to the hole must be larger than 3 times the diameter of the hole. So the whole length of the sample must be larger than 7 times the hole's diameter, which means the minimum is 70 mm. Moreover, the height should be twice the width during uniaxial compression [43]. Therefore, the minimum sample size has to be 70 mm × 70 mm × 140 mm. The slurry was poured into a 70 mm × 70 mm × 140 mm steel mold, in the center of which a prefabricated drilling device with a drilling radius of 5 mm was placed, as shown in Figure 1. The sample was shaken appropriately to remove any air bubbles in the slurry. It was removed from the mold after 12 h and placed in a ventilated location for 28 d. The coefficients of variation (i.e., ratio of the standard deviation to the mean) of the uniaxial compressive strength, peak strain (i.e., the strain corresponding to the peak stress), and elastic modulus of the samples were 2.03%, 1.44%, and 3.06%, respectively, indicating that the prepared samples had stable mechanical properties. The dimensions of the hole (φ), the uniaxial compressive strength (UCS), and the test parameters of the samples are presented in Table 1.

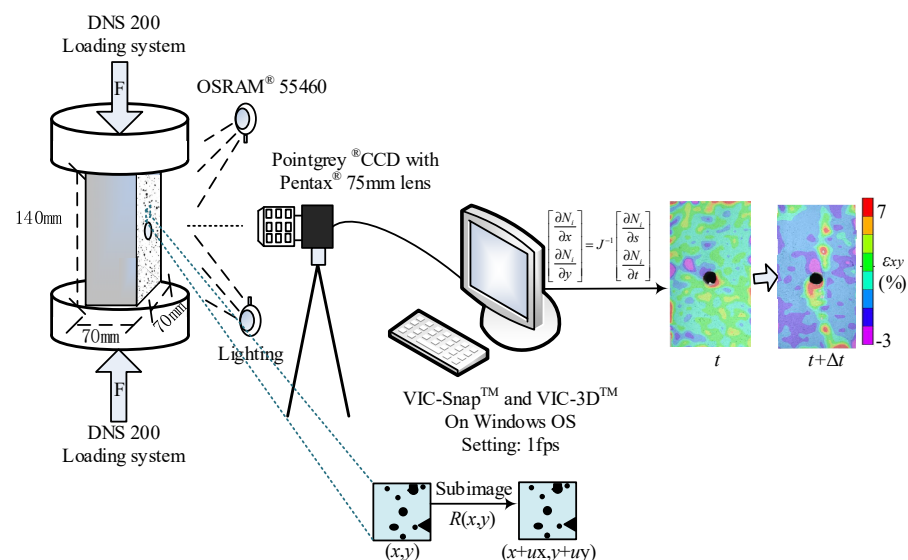


Figure 1. Assembly of test system.

Table 1. Sample size and test parameters.

Sample	Mass (g)	Size (mm)	φ (mm)	UCS (MPa)	E (MPa)
SH-1	897.10	70.3 × 70.1 × 140.5	10	1.53	329.95
SH-2	886.23	70.4 × 70.2 × 140.3	10	1.48	310.02
SH-3	894.56	70.0 × 70.6 × 140.2	10	1.55	332.23

2.2. Testing Method

The testing system consisted of a loading system and a digital image observation system as shown in Figure 1. The loading system was a DNS-200 electronic universal testing machine (Changchun Machinery Research Institute Co., Ltd., Changchun, China), which can be used for laboratory testing of non-metallic materials. The tests were conducted under uniaxial compression, which was through displacement-controlled loading at a loading rate of 0.05 mm/min, and the loading was continued until the sample failed. The digital image observation system consisted of image acquisition and processing devices. This system can collect the images of the surface of the sample in real time, store the image in the disk in digital form, which was used to calculate the full-field strain, and output it with a matrix.

2.3. Energy Calculation

In this paper, the total energy U , elastic strain energy U_e , and dissipated energy U_d are investigated during the experiment, which can be derived from Appendix A. As the strain is the key value to calculate the energy, to get the strain field on the surface of the sample, perform the image correlation calculation by matching the image before and after deformation. First, traverse all the regions of the two images to obtain the correlation coefficient C . One of the typical correlation coefficients was noted as [50]:

$$C = \int_R [f(x) - g(\Phi(x))]^2 dx = \int_R [f(x) - g(x + u_0(x))]^2 dx \quad (1)$$

where x was the gray level, $f(x)$ was the distribution of the image before deformation, $g(x)$ was the distribution of the image after deformation, and R was the interesting area.

Compare the pixel of the two images to get displacement as shown in Figure 1. Then, the strain field can be obtained by differencing the displacement field. That needs selecting a small area near the measuring point, fitting the displacement to get a plane, and building a local coordinate system with the origin at the point. Through the above operations, all the displacement of the sample was translated into this local coordinate, and the difference was performed to get the components of strain. A typical difference equation is shown in Appendix B.

3. Results and Discussion

3.1. Failure Modes of Samples Containing Holes

Three basic types of cracks, namely, tensile cracks (T), shear cracks (S), and remote cracks (R), were observed during the deformation and fracturing of the samples containing holes under pressure as shown in Figure 2. The failure mode was shear failure, and the specific failure processes were as follows. The initial tensile cracks first appeared in the upper and lower ends of the hole boundary but did not propagate to the edge of the sample. Then, shear cracks occurred on the left and right sides of the hole boundary, and remote cracks (essentially tensile cracks) appeared at the remote end of the hole boundary. With continuous loading, the initial shear cracks propagated and coalesced with the remote cracks to form macroscopic shear failure cracks, resulting in diagonal shear failure. This finding is consistent with the result of the progressive fracturing process [2,41]. However, we found that there was another type of crack where the remote cracks and shear cracks merge and that the formation of such cracks is caused by the combined action of the tensile stress and shear cracks [42]. This phenomenon has been discussed in the research related to fracture coalescence [51].

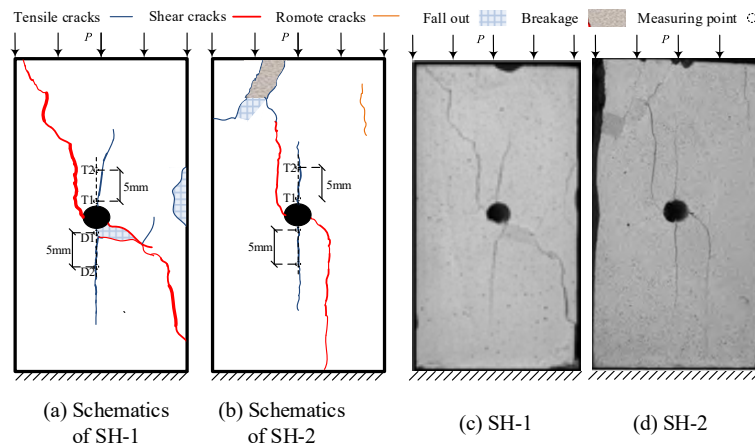


Figure 2. Sample failure modes: (a) Schematics of SH-1, (b) Schematics of SH-2, (c) SH-1, and (d) SH-2.

3.2. Evolution of Horizontal Strain of Tensile Cracks

During loading, energy dissipation causes damage to the interior of the sample, resulting in the deterioration or loss of the strength of the sample. Therefore, the energy dissipation is closely related to the degradation of the sample strength. All the values of energy at the peak stress were show in Table 2. Based on the variations in the dissipated energy of the samples containing holes, the deformation and failure process of the samples containing holes was divided into four stages: an initial dissipation stage, a decelerated energy stage, a stable dissipation stage, and an accelerated dissipations stage, as shown in Figure 3.

Table 2. Energy values at the peak stress.

Sample	Total Energy (MJ·cm ⁻³)	Elastic Strain Energy (MJ·cm ⁻³)	Dissipated Energy (MJ·cm ⁻³)	Proportion of Dissipated Energy
SH-1	0.411	0.3034	0.1076	26.19%
SH-2	0.382	0.315	0.0930	24.34%
SH-3	0.377	0.2865	0.0905	24.26%

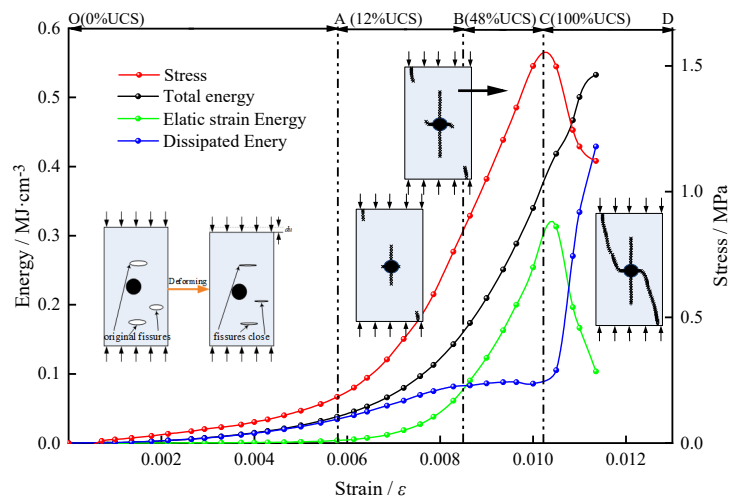


Figure 3. Comparison of energy conversion and stress of SH-1 during the uniaxial compression test. OA: initial dissipation stage, AB: decelerated energy dissipation stage, BC: stable dissipation stage, CD: accelerated dissipation stage. (Schematics based on the images captured with VIC-Snap).

In the initial dissipation stage, the energy is dissipated due to the closure and friction of the micro-fissures and the empty micro-gaps inside the sample, and the energy dissipation curve slowly increases with the generation of micro-deformation. The elastic strain energy also increases gradually but slightly as the deformation increases, which is attributed to the energy dissipation due to the initiation and development of micro-fissures. This is consistent with the results of previous studies [52], that is, the more fully the fissures develop, the larger the proportion of the dissipated energy absorbed by the sample is.

In the decelerated energy dissipation stage, the deformation of the sample increases. The original fissures and the new micro-fissures gradually close, causing the effective contact area inside the sample and the accumulation rate of the elastic strain energy to increase and causing the growth rate of the dissipated energy to gradually decrease. However, the dissipated energy is still larger than the elastic energy in section AB, indicating that some of the micro-fissures reopen. When the loading reaches 48% of the peak stress, the dissipated energy is still greater than the elastic energy. This phenomenon differs from the energy conversion of intact homogeneous samples of coal, sandstone, and granite [53]. This phenomenon is noteworthy and was analyzed in detail in this study. In previous studies [54,55], it was found that after the compaction stage, localized concentration occurs at the upper and lower ends of the hole boundary under tensile stress. According to the maximum tensile strain criterion, it is concluded that micro-fractures are formed in the upper and lower regions around the hole, but they have a low density and do not nucleate to form macroscopic failure cracks. Thus, it is concluded that the dissipated energy is greater than the elastic strain energy before 48% of the peak stress is reached due to the continuous development and migration of micro-fissures in the upper and lower regions around the hole.

When coming into the stable dissipation stage, after the elastic strain energy curve intersects with the dissipated energy curve, the growth rate of the elastic strain energy increases rapidly and is consistent with the rate of the total energy input to the system. At this time, a large proportion of the total energy input is converted into elastic strain energy and is stored in the sample. The dissipated energy is essentially stable at approximately $0.1 \text{ MJ}\cdot\text{cm}^{-3}$ and accounts for 25% of the energy. According to the fracture pattern of the coal-rock mass around the hole, the fractures in the upper and lower regions around the hole continue to develop and propagate, forming a tensile macro-crack parallel to the loading direction. In addition, cracks also begin to appear on the left and right sides of the hole boundary, as well as at the remote end of the hole. Thus, it is concluded that in the stable dissipation stage, a quarter of the energy still becomes dissipated energy, forming a tensile macro-crack in the upper and lower ends around the hole.

In the accelerated dissipation stage, the peak strength is reached, the elastic strain energy accumulated in the sample is rapidly released, the elastic strain energy decreases quickly, and the dissipated energy increases rapidly as the strain increases. As a result, the shear cracks and remote cracks propagate rapidly and coalesce to form the final failure mode.

3.3. Evolution of Horizontal Strain of Tensile Cracks

During the fracturing of the samples containing holes, the tensile cracks are not macro-cracks and stop developing after reaching a certain length, and the samples finally fail along a diagonal shear macro-crack. To further describe the influence of the dissipated energy on the evolution of the tensile cracks, the measuring points were arranged at a spacing of 5 mm between the upper and lower ends of the borehole and were numbered D1, D2, T1, and T2 as shown in Figure 2, based on the method used to analyze the fracturing of a horseshoe-shaped cavity [56]. The changes in the horizontal strain ε_x during the compression process were measured.

Quantitative analysis was conducted at points T1, T2, D1, and D2. The dissipated energy and deformation of the horizontal strain at each measuring point with time during the failure process are shown in Figure 4.

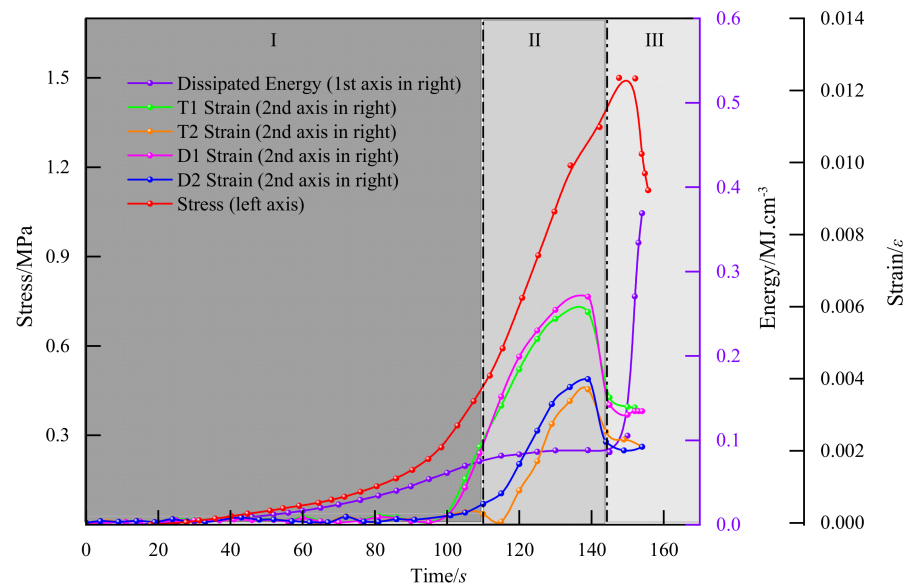


Figure 4. Dissipated energy and deformation of SH-1 during the uniaxial compression test. I: Slow rise stage of horizontal strain; II: Rapid change stage of horizontal strain; III: Smooth stage of horizontal strain.

The energy dissipation and tensile crack propagation of the samples containing holes were analyzed. In the initial stage of loading (before 78 s), the horizontal strain at each measurement point was relatively stable, with a strain of less than 2×10^{-3} . The tensile cracks in the upper and lower ends of the hole were initiated at almost the same time. After that, the horizontal strain at measurement points 1 and 2 increased rapidly and maintained this growth rate for some time. The tensile cracks in the upper and lower ends of the hole continued to propagate to a point at 121 s, and the growth rate decreased, significantly reducing the magnitude of the increase. When the loading reached 132 s, the horizontal strain reached its maximum and then decreased to a low level, indicating that closure of the cracks in the upper and lower ends of the hole occurred at point III. The horizontal strain at measurement points 3 and 4 reached the peak at 135 s and then decreased rapidly. The horizontal strain at these measurement points dropped to a certain low level and remained almost stable in the subsequent stage. According to the test results, the final strain at each of the four measurement points was still slightly larger than the corresponding initial horizontal strain, and there was still residual strain around each measurement point. When the deformation continues to increase, the horizontal strain at each measurement point increases, indicating the reopening of the tensile cracks.

It can be seen from the above analysis that during the loading process, the tensile cracks in the upper and lower ends of the samples containing holes underwent an opening–closing–reopening process.

3.4. Analysis of Energy Dissipation and Horizontal Strain

The initial tensile cracks essentially had no influence on the macroscopic failure mode of the samples containing holes. The above analysis shows that the amount of dissipated energy released was closely related to the propagation of the tensile cracks. Figure 5 compares the tensile cracks and dissipated energy. At the end of the compaction stage, as the dissipated energy increased, the initial tensile micro-cracks continuously initiated, developed, and opened, and thus, the transverse strain of the initial tensile cracks increased continuously. From 115 s to 125 s, the dissipated energy increased slightly, and the horizontal strain of the tensile cracks increased rapidly, indicating that the generated dissipated energy was all used for the development of the tensile cracks. From 125 s to 140 s, the dissipated energy only changed slightly, and the growth rate of the horizontal

strain of the tensile cracks slowed down. This occurred because the dissipated energy was also used for the initiation and development of the cracks to the left and right sides of the hole (subjected to compressive shear stress) and the remote cracks. In addition, this also shows that after the loading reached a certain extent, the energy input into the sample by the testing machine was mainly stored in the sample in the form of elastic energy, which is also applicable to samples containing pores. Therefore, the generation of remote cracks and cracks to the left and right of the hole boundary inhibited the propagation of the tensile cracks, corresponding to the closed state in this stage. Subsequently, when the energy storage limit was reached, the elastic strain energy stored around the hole was released, and the macroscopic failure cracks propagated and coalesced, causing the stress environment to change. At this time, the initial tensile cracks, which were previously in a closed state due to inhibition, propagated again and finally formed tensile cracks.

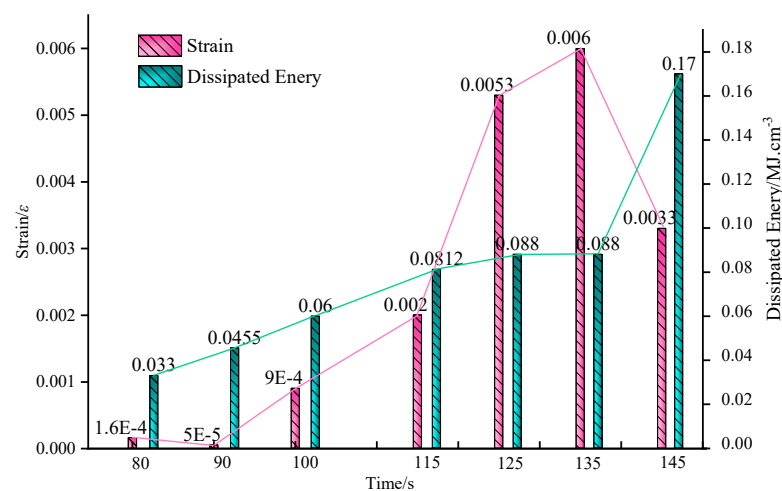


Figure 5. Comparison of dissipated energy and horizontal strain of the tensile cracks of SH-1 during the uniaxial compression test.

3.5. Mechanism of Tensile Crack Inhibition

The distribution of the crack in this experiment shown in Figure 2 again confirmed the three types of cracks which are remote, primary, and shear [2,38,42,57]. Here, the dissipated energy is greater than the elastic strain energy before 48% of the peak stress, while the primary tensile crack propagates as shown in Figure 3. The primary tensile crack would be the early symptom of the sample's or the gas drainage borehole's failure. Thus, the primary tensile crack should be the research with the highest priority.

As mentioned in Figure 3, the initial cracks and crack tips were formed by a series of short tensile cracks [58]. The tensile cracks in the upper and lower ends of the samples had an opening–closing–reopening process, as shown in Figure 4. This process is illustrated in Figure 6. The tensile crack propagation was accompanied by the generation and migration of three specific zones: the fracture propagation zone, friction zone, and intact zone. The appearance of the fracture propagation zone represents the generation of the initial cracks, followed by continuous extension and propagation to form the entire macro-crack. The friction zone is formed after the appearance of the fracture initiation zone and is mainly located where the friction between the fracture surfaces resists the failure of the rock. In the intact zone, the rock material remains intact, and the shear force is mainly provided by the cohesion. As the loading progresses and the cracks gradually propagate, the friction zone gradually increases, while the intact zone gradually decreases, reflecting the process in which the cohesion of the rock is gradually replaced by the friction between the fracture surfaces.

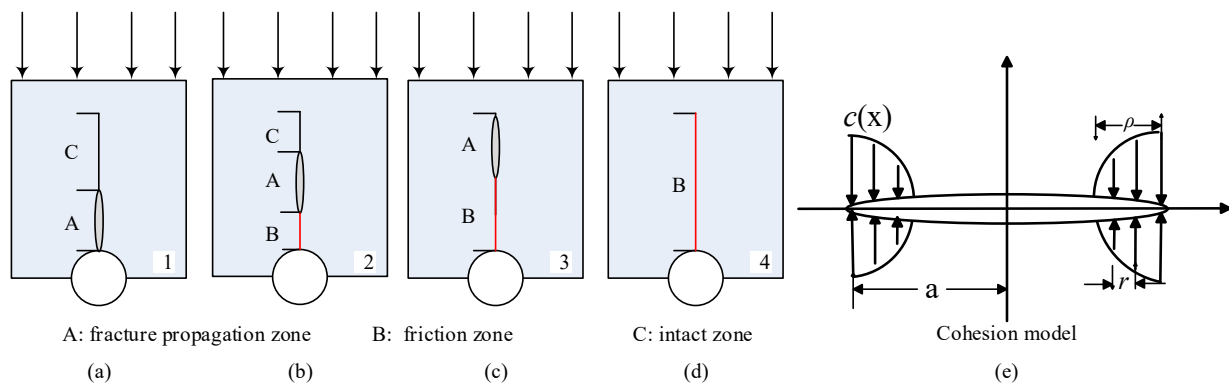


Figure 6. Tensile crack propagation process. (a) initial cracks with the fracture propagation zone appearance, (b) cracks propagation with friction zone forming, (c) the friction between the fracture surfaces resists the cracks propagation with intact zone disappearance, (d) cohesion of the rock replaced by the friction between the fracture surfaces with fracture propagation zone disappearance, and (e) cohesion model.

Though the stress field distribution at the tensile crack tip exhibited a similar pattern, not all of the distributions at the ends exhibited extended patterns in the actual observations of the plastic zone at the crack tips. Specifically, for a structure containing holes, the primary tensile crack caused by the concentration of the tensile stress at the upper and lower ends of the hole began to propagate, which can be expressed as [5]:

$$\sigma_t = K_{IC}(\pi a)^{-1/2} \quad (2)$$

where K_{IC} is the tensile stress intensity factor, and a is half of the crack length.

The above equation can also be written as

$$K_{IC} = \sigma_t \sqrt{\pi a} \quad (3)$$

For the case in which tensile stress is applied perpendicular to a set of equally spaced coplanar cracks, the strength of the rock σ_t can be expressed as:

$$\sigma_t = K_{IC} \sqrt{2b} \left(t g \frac{\pi a}{2b} \right)^{-1/2} \quad (4)$$

where $2b$ is the distance from the center of the crack.

During the development of the initial primary tensile crack, the crack's tip produces a damping effect at the leading edge. That is, within the range of the tip, the distance between the fracture surfaces is very small, and the cohesion between the molecules or atoms present on the fracture surfaces does not disappear completely, which is an important factor that must be considered.

As shown in Figure 6e, according to the cohesion model, the stress intensity factor K_I' corresponding to the cohesion $c(x)$ is proposed to be [5]:

$$K_I' = -2 \sqrt{\frac{a}{\pi}} \int_0^a \frac{c(x) dx}{\sqrt{a^2 - x^2}} \quad (5)$$

where r is the cohesion decay distance starting from the molecular dislocation point. Since $c(x)$ only exists within a very small local area ρ at the crack's tip, and $\rho \ll a$, $r \leq \rho \leq a$, and $a^2 - x^2 = (a + x)(a - x) = (2a - r)r = 2ar$.

Substituting the above relationship into Equation (5) and transforming the integration variable yields

$$K_I' = -2 \sqrt{\frac{a}{\pi}} \int_0^\rho \frac{c(r)}{\sqrt{r}} dr, r \in [0, \rho] \quad (6)$$

From the above theoretical analysis, it can be seen that the cohesion $c(x)$ does produce resistance to crack propagation and reduces the singularity of the stresses in the region, which produces results similar to those of the tensile stress and reduces the tensile stress intensity factor K_I at the crack's tip. This is in general agreement with the change trend of the stress field environment that leads to the inhibition of the further propagation of the tensile cracks. It was found that the stress intensity factor at the crack's tip decreased during crack propagation, which was favorable to the connection and coalescence of the other cracks.

4. Conclusions

According to the variations in the dissipated energy, the failure process of the samples containing holes was divided into an initial dissipation stage, a decelerated dissipation stage, a stable dissipation stage, and an accelerated dissipation stage. During the first half of loading, the initial tensile cracks developed continuously, and the dissipated energy was greater than the elastic energy.

The amount of dissipated energy released was closely related to the propagation of the tensile cracks. In the early stage, almost all the dissipated energy was used for the development and expansion of the tensile cracks. In the middle stage, the generation of remote cracks and cracks to the left and right of the hole boundary inhibited the propagation of the tensile cracks. In the later stage, the energy storage limit was reached, the elastic strain energy around the hole was released, and the macroscopic failure cracks propagated and coalesced, which changed the stress environment and caused the tensile cracks to reopen and finally develop.

The tensile cracks in the upper and lower ends of the samples containing holes experienced an opening–closing–reopening process. The presence of cohesion $c(x)$ hindered the propagation of the tensile cracks, which were formed by the generation and migration of the fracture propagation zone, friction zone, and intact zone.

The energy evolution of the coal–rock mass around the hole was investigated in this paper. The dissipated energy released was related to the propagation of the tensile cracks, revealing the three stages of the propagation. This could be used for the gas drainage borehole structure monitor and predicting potential flaws. Future work will focus on building the relationship between the dissipated energy and the tensile crack. Investigating the energy evolution during the shear crack propagation will be another issue.

Author Contributions: Conceptualization, C.J.; methodology, C.J.; software, C.J.; validation, L.Z.; formal analysis, C.J.; investigation, C.J.; resources, C.J.; data curation, C.J.; writing—original draft preparation, C.J.; writing—review and editing, L.Z.; visualization, C.J. and L.Z.; supervision, L.Z.; project administration, L.Z.; funding acquisition, L.Z. All authors have read and agreed to the published version of the manuscript.

Funding: This research was funded by [National Natural Science Foundation of China] grant number [52104216], and [China Postdoctoral Science Foundation] grant number [2020M683680XB]. The APC was funded by [National Natural Science Foundation of China].

Institutional Review Board Statement: Not applicable.

Informed Consent Statement: Not applicable.

Data Availability Statement: The data presented in this study are available on request from the corresponding author.

Conflicts of Interest: The authors declare no conflict of interest.

Appendix A

The energy dissipates and is released from the rock mass during the progress from deformation to failure. According to the first law of thermodynamics [53,59],

$$U^d = U - U^e \quad (A1)$$

where U is the total input energy generated by the external work; U^d is the dissipated energy; and U^e is the releasable elastic strain energy.

According to thermodynamics, energy dissipation is unidirectional and irreversible, while energy release is reversible under certain conditions. In the principal stress space, the unit energy of the coal–rock mass is expressed as follows [60]:

$$U = \int_0^{\varepsilon_1} \sigma_1 d\varepsilon_1 + \int_0^{\varepsilon_2} \sigma_2 d\varepsilon_2 + \int_0^{\varepsilon_3} \sigma_3 d\varepsilon_3 \quad (A2)$$

$$U^e = \frac{1}{2}\sigma_1\varepsilon_1^e + \frac{1}{2}\sigma_2\varepsilon_2^e + \frac{1}{2}\sigma_3\varepsilon_3^e \quad (A3)$$

According to Hooke's law, Equation (3) can be rewritten as

$$U^e = \frac{1}{2E_i}(\sigma_1^2 + \sigma_2^2 + \sigma_3^2) - \frac{\nu}{E_i}(\sigma_1\sigma_2 + \sigma_2\sigma_3 + \sigma_1\sigma_3) \quad (A4)$$

where ν is Poisson's ratio, and E_i is the unloading elastic modulus.

For the convenience of calculation, the initial elastic modulus E_0 is generally used to replace E_i . The elastic strain energy under uniaxial compression conditions can be calculated as follows [61]:

$$U^e = \frac{1}{2}\sigma_i(\varepsilon_i - \varepsilon_d) = \frac{1}{2E_0}\sigma_i^2 \quad (A5)$$

where ε_i is the strain corresponding to σ_i ; and ε_d is the residual permanent strain when the stress is unloaded from σ_i to $\sigma = 0$.

Thus, the total energy can be calculated as follows:

$$U = \int_{\varepsilon_1}^{\varepsilon_2} \sigma d\varepsilon = \sum_{i=1}^{n-1} \int_{\varepsilon_i}^{\varepsilon_{i+1}} \sigma_i d\varepsilon = \sum_{i=1}^{n-1} \frac{1(\varepsilon_{i+1} - \varepsilon_i)}{2}(\sigma_{i+1} + \sigma_i) \quad (A6)$$

where σ_i^i and ε_i^i are the stress and strain at each point on the stress curve, respectively.

Finally, the dissipated energy U^d of the sample during the test is obtained by Equations (A1), (A5) and (A6).

Appendix B

$$\begin{aligned} \varepsilon_{11} &= \frac{\partial d_1}{\partial X_1} + \frac{1}{2} \left[\left(\frac{\partial d_1}{\partial X_1} \right)^2 + \left(\frac{\partial d_2}{\partial X_1} \right)^2 + \left(\frac{\partial d_3}{\partial X_1} \right)^2 \right] \\ \varepsilon_{22} &= \frac{\partial d_2}{\partial X_2} + \frac{1}{2} \left[\left(\frac{\partial d_1}{\partial X_2} \right)^2 + \left(\frac{\partial d_2}{\partial X_2} \right)^2 + \left(\frac{\partial d_3}{\partial X_2} \right)^2 \right] \\ \varepsilon_{33} &= \frac{\partial d_3}{\partial X_3} + \frac{1}{2} \left[\left(\frac{\partial d_1}{\partial X_3} \right)^2 + \left(\frac{\partial d_2}{\partial X_3} \right)^2 + \left(\frac{\partial d_3}{\partial X_3} \right)^2 \right] \\ \varepsilon_{12} &= \frac{1}{2} \left(\frac{\partial d_1}{\partial X_2} + \frac{\partial d_2}{\partial X_1} \right) + \frac{1}{2} \left[\left(\frac{\partial d_1}{\partial X_1} \frac{\partial d_1}{\partial X_2} \right) + \left(\frac{\partial d_2}{\partial X_1} \frac{\partial d_2}{\partial X_2} \right) + \left(\frac{\partial d_3}{\partial X_1} \frac{\partial d_3}{\partial X_2} \right) \right] \\ \varepsilon_{23} &= \frac{1}{2} \left(\frac{\partial d_2}{\partial X_3} + \frac{\partial d_3}{\partial X_2} \right) + \frac{1}{2} \left[\left(\frac{\partial d_1}{\partial X_2} \frac{\partial d_1}{\partial X_3} \right) + \left(\frac{\partial d_2}{\partial X_2} \frac{\partial d_2}{\partial X_3} \right) + \left(\frac{\partial d_3}{\partial X_2} \frac{\partial d_3}{\partial X_3} \right) \right] \\ \varepsilon_{31} &= \frac{1}{2} \left(\frac{\partial d_3}{\partial X_1} + \frac{\partial d_1}{\partial X_3} \right) + \frac{1}{2} \left[\left(\frac{\partial d_1}{\partial X_3} \frac{\partial d_1}{\partial X_1} \right) + \left(\frac{\partial d_2}{\partial X_3} \frac{\partial d_2}{\partial X_1} \right) + \left(\frac{\partial d_3}{\partial X_3} \frac{\partial d_3}{\partial X_1} \right) \right], \end{aligned} \quad (A7)$$

where ε_{11} , ε_{22} , ε_{33} , ε_{12} , ε_{23} , and ε_{31} are the Lagrangian strain tensor, d_1 , d_2 , and d_3 are the displacement in three directions, and X_1 , X_2 , and X_3 are the position of the point.

References

1. Lajtai, E.Z. Brittle fracture in compression. *Int. J. Fract.* **1974**, *10*, 525–536. [CrossRef]
2. Lajtai, E.Z.; Lajtai, V.N. The collapse of cavities. *Int. J. Rock Mech. Min. Sci. Geomech. Abstr.* **1975**, *12*, 81–86. [CrossRef]
3. Nguyen, K.D.; Thanh, C.-L.; Vogel, F.; Nguyen-Xuan, H.; Abdel-Wahab, M. Crack propagation in quasi-brittle materials by fourth-order phase-field cohesive zone model. *Theor. Appl. Fract. Mech.* **2022**, *118*, 103236. [CrossRef]
4. Dzik, E.J.; Lajtai, E.Z. Primary fracture propagation from circular cavities loaded in compression. *Int. J. Fract.* **1996**, *79*, 49–64. [CrossRef]

5. Barenblatt, G.I. Scaling Phenomena in Fatigue and Fracture. *Int. J. Fract.* **2006**, *138*, 19. [[CrossRef](#)]
6. Botvina, L.R. The Benefits and Challenges of Interdisciplinary Research. *Phys. Mesomech.* **2019**, *22*, 5–12. [[CrossRef](#)]
7. Liaghat, F.; Hematiyan, M.R.; Khosravifard, A.; Rabczuk, T. A robust meshfree method for analysis of cohesive crack propagation problems. *Theor. Appl. Fract. Mech.* **2019**, *104*, 102328. [[CrossRef](#)]
8. Javanmardi, M.R.; Maheri, M.R. Extended finite element method and anisotropic damage plasticity for modelling crack propagation in concrete. *Finite Elem. Anal. Des.* **2019**, *165*, 1–20. [[CrossRef](#)]
9. Dirik, H.; Yalçinkaya, T. Crack path and life prediction under mixed mode cyclic variable amplitude loading through XFEM. *Int. J. Fatigue* **2018**, *114*, 34–50. [[CrossRef](#)]
10. Carpinteri, A.; Cornetti, P.; Barpi, F.; Valente, S. Cohesive crack model description of ductile to brittle size-scale transition: Dimensional analysis vs. renormalization group theory. *Eng. Fract. Mech.* **2003**, *70*, 1809–1839. [[CrossRef](#)]
11. Carter, B.J.; Lajtai, E.Z.; Yuan, Y. Tensile fracture from circular cavities loaded in compression. *Int. J. Fract.* **1992**, *57*, 221–236. [[CrossRef](#)]
12. Carpinteri, A.; Chiaia, B.; Cornetti, P. A scale-invariant cohesive crack model for quasi-brittle materials. *Eng. Fract. Mech.* **2002**, *69*, 207–217. [[CrossRef](#)]
13. Gea dos Santos, F.L.; Forti, T.L.D. Concrete cohesive curves for specimens with different sizes: A study of inverse analysis and size effect. *Eng. Fract. Mech.* **2022**, *261*, 108249. [[CrossRef](#)]
14. Bažant, Z.P.; Yavari, A. Is the cause of size effect on structural strength fractal or energetic–statistical? *Eng. Fract. Mech.* **2005**, *72*, 1–31. [[CrossRef](#)]
15. Bulat, A.; Osinnii, V.; Dreus, A.; Osinnia, N. Mathematical modelling of thermal stresses within the borehole walls in terms of plasma action. *Min. Miner. Depos.* **2021**, *15*, 63–69. [[CrossRef](#)]
16. Kulynych, V.; Chebenko, V.; Puzyr, R.; Pieieva, I. Modelling the influence of gaseous products of explosive detonation on the processes of crack treatment while rock blasting. *Min. Miner. Depos.* **2021**, *15*, 102–107. [[CrossRef](#)]
17. Jia, Z.Q.; Xie, H.P.; Zhang, R.; Li, C.B.; Wang, M.; Gao, M.Z.; Zhang, Z.P.; Zhang, Z.T. Acoustic Emission Characteristics and Damage Evolution of Coal at Different Depths Under Triaxial Compression. *Rock Mech. Rock Eng.* **2020**, *53*, 2063–2076. [[CrossRef](#)]
18. Peng, R.D.; Ju, Y.; Wang, J.G.; Xie, H.P.; Gao, F.; Mao, L.T. Energy Dissipation and Release During Coal Failure Under Conventional Triaxial Compression. *Rock Mech. Rock Eng.* **2015**, *48*, 509–526. [[CrossRef](#)]
19. Xie, H.P.; Xie, J.; Gao, M.Z.; Zhang, R.; Zhou, H.W.; Gao, F.; Zhang, Z.T. Theoretical and experimental validation of mining-enhanced permeability for simultaneous exploitation of coal and gas. *Environ. Earth Sci.* **2015**, *73*, 5951–5962. [[CrossRef](#)]
20. Zhizhen, Z.; Feng, G. Research on nonlinear characteristics of rock energy evolution under uniaxial compression. *Chin. J. Rock Mech. Eng.* **2012**, *31*, 1198–1207.
21. Ju, Y.; Li, Y.; Xie, H.; Song, Z.; Tian, L. Stress wave propagation and energy dissipation in jointed rocks. *Chin. J. Rock Mech. Eng.* **2006**, *25*, 2426–2434.
22. Zhang, T.-J.; Zhang, L.; Li, S.-G.; Liu, J.-L.; Pan, H.-Y.; Ji, X. Wave Velocity and Power Spectral Density of Hole-Containing Specimens with Different Moisture Content under Uniaxial Compression. *Energies* **2018**, *11*, 3166. [[CrossRef](#)]
23. Yangsheng, Z.; Zengchao, F.; Zhijun, W. Least energy principle of dynamical failure of rock mass. *Chin. J. Rock Mech. Eng.* **2003**, *22*, 1781–1783.
24. Kong, X.G.; Wang, E.Y.; Li, S.G.; Lin, H.F.; Xiao, P.; Zhang, K.Z. Fractals and chaos characteristics of acoustic emission energy about gas-bearing coal during loaded failure. *Fractals-Complex Geom. Patterns Scaling Nat. Soc.* **2019**, *27*, 1950072. [[CrossRef](#)]
25. Lai, X.; Ren, J.; Cui, F.; Shan, P.; Dai, J.; Xu, H.; Wang, Z. Study on vertical cross loading fracture of coal mass through hole based on AE-TF characteristics. *Appl. Acoust.* **2020**, *166*, 107353. [[CrossRef](#)]
26. Wang, X.R.; Liu, X.D.; He, T.; Xiao, D.H.; Shan, Y.C. Structural damage acoustic emission information enhancement through acoustic black hole mechanism. *Measurement* **2022**, *190*, 110673. [[CrossRef](#)]
27. Mirsayar, M. A generalized model for dynamic mixed-mode fracture via state-based peridynamics. *Fatigue Fract. Eng. Mater. Struct.* **2022**, *in press*. [[CrossRef](#)]
28. Jang, Y.; Wang, T.; Chen, T.; Bai, X.; Xie, S. Features of coal bumps influenced by normal faults in coal mining with hard roof and hard coal. *Chin. J. Rock Mech. Eng.* **2013**, *32*, 3712–3718.
29. Zhang, J.; Li, Y.W.; Pan, Y.S.; Wang, X.Y.; Yan, M.S.; Shi, X.D.; Zhou, X.J.; Li, H.L. Experiments and analysis on the influence of multiple closed cemented natural fractures on hydraulic fracture propagation in a tight sandstone reservoir. *Eng. Geol.* **2021**, *281*, 105981. [[CrossRef](#)]
30. Liu, C.; Huang, X.S.; Yue, W.P.; Zhang, C. Extension of grouting-induced splitting fractures in materials similar to coal rocks containing prefabricated fractures. *J. Geophys. Eng.* **2020**, *17*, 670–685. [[CrossRef](#)]
31. Navidtehrani, Y.; Betegón, C.; Martínez-Pañeda, E. A general framework for decomposing the phase field fracture driving force, particularised to a Drucker–Prager failure surface. *Theor. Appl. Fract. Mech.* **2022**, *121*, 103555. [[CrossRef](#)]
32. Mirsayar, M.M. Mixed mode fracture analysis using extended maximum tangential strain criterion. *Mater. Des.* **2015**, *86*, 941–947. [[CrossRef](#)]
33. Mirsayar, M.M. On the effective critical distances in three-dimensional brittle fracture via a strain-based framework. *Eng. Fract. Mech.* **2021**, *248*, 107740. [[CrossRef](#)]
34. Wang, Q.; Feng, Y.T.; Zhou, W.; Cheng, Y.; Ma, G. A phase-field model for mixed-mode fracture based on a unified tensile fracture criterion. *Comput. Methods Appl. Mech. Eng.* **2020**, *370*, 113270. [[CrossRef](#)]

35. Svolos, L.; Mourad, H.M.; Manzini, G.; Garikipati, K. A fourth-order phase-field fracture model: Formulation and numerical solution using a continuous/discontinuous Galerkin method. *J. Mech. Phys. Solids* **2022**, *165*, 104910. [[CrossRef](#)]
36. Han, Y.; Zhang, F.; Liu, X.; Li, X. Numerical simulation of instability and failure types of coalbed borehole based on Hoek-Brown criterion. *Meitan Xuebao J. China Coal Soc.* **2020**, *45*, 308–318. [[CrossRef](#)]
37. Martin, C.D.; Chandler, N.A. Progressive fracture of Lac du Bonnet granite. *Int. J. Rock Mech. Min. Sci.* **1994**, *31*, 643–659. [[CrossRef](#)]
38. Zhang, T.; Zhang, L.; Li, S.; Zhang, C.; Song, S.; Bao, R. Characteristics of the surface deformation of specimens with a hole during the progressive failure. *Meitan Xuebao J. China Coal Soc.* **2017**, *42*, 2623–2630. [[CrossRef](#)]
39. Sammis, C.G.; Ashby, M.F. The failure of brittle porous solids under compressive stress states. *Acta Metall.* **1986**, *34*, 511–526. [[CrossRef](#)]
40. Tang, C.A.; Wong, R.H.C.; Chau, K.T.; Lin, P. Modeling of compression-induced splitting failure in heterogeneous brittle porous solids. *Eng. Fract. Mech.* **2005**, *72*, 597–615. [[CrossRef](#)]
41. Zhu, W.C.; Liu, J.; Tang, C.A.; Zhao, X.D.; Brady, B.H. Simulation of progressive fracturing processes around underground excavations under biaxial compression. *Tunn. Undergr. Space Technol.* **2005**, *20*, 231–247. [[CrossRef](#)]
42. Zhang, T.; Jing, C.; Zhang, L.; Ji, X.; Pang, H. Strain localization characteristics of perforation failure of perforated specimens. *J. China Coal Soc.* **2020**, *45*, 4087–4094. [[CrossRef](#)]
43. Zhang, T.; Zhang, L.; Li, S.; Liu, J.; Pan, H.; Song, S. Stress Inversion of Coal with a Gas Drilling Borehole and the Law of Crack Propagation. *Energies* **2017**, *10*, 1743. [[CrossRef](#)]
44. Liu, Z.; Li, X.; Li, Z.; Liu, Y.; Yang, Y.; Feng, J. Electric potential of the hole wall of concrete under uniaxial compression. *J. China Coal Soc.* **2014**, *39*, 372–377. [[CrossRef](#)]
45. Dong, J.-Y.; Yang, J.-H.; Yang, G.-X.; Wu, F.-Q.; Liu, H.-S. Research on similar material proportioning test of model test based on orthogonal design. *Meitan Xuebao J. China Coal Soc.* **2012**, *37*, 44–49.
46. Zhao, B.; Wen, G.; Sun, H.; Sun, D.; Yang, H.; Cao, J.; Dai, L.; Wang, B. Similarity criteria and coal-like material in coal and gas outburst physical simulation. *Int. J. Coal Sci. Technol.* **2018**, *5*, 167–178. [[CrossRef](#)]
47. Zhang, L.; Jing, C.; Li, S.; Bao, R.; Zhang, T. Seepage Law of Nearly Flat Coal Seam Based on Three-Dimensional Structure of Borehole and the Deep Soft Rock Roadway Intersection. *Energies* **2022**, *15*, 5012. [[CrossRef](#)]
48. Skipochka, S.; Krukovskiy, O.; Palamarchuk, T.; Prokhorets, L. On the methodology for considering scale effect of rock strength. *Min. Miner. Depos.* **2020**, *14*, 24–30. [[CrossRef](#)]
49. Wang, S.; Guo, W. Chapter 5—Structural effect of rock blocks. In *Scale-Size and Structural Effects of Rock Materials*; Wang, S., Masoumi, H., Oh, J., Zhang, S., Eds.; Woodhead Publishing: Sawston, UK, 2020; pp. 495–633.
50. Schreier, H.; Ortu, J.-J.; Sutton, M.A. *Image Correlation for Shape, Motion and Deformation Measurements: Basic Concepts, Theory and Applications*; Springer: New York, NY, USA, 2009; pp. 1–321.
51. Renard, F.; McBeck, J.; Cordonnier, B.; Zheng, X.J.; Kandula, N.; Sanchez, J.R.; Kobchenko, M.; Noiri, C.; Zhu, W.L.; Meakin, P.; et al. Dynamic In Situ Three-Dimensional Imaging and Digital Volume Correlation Analysis to Quantify Strain Localization and Fracture Coalescence in Sandstone. *Pure Appl. Geophys.* **2019**, *176*, 1083–1115. [[CrossRef](#)]
52. Li, H.; Zhou, H.; Jiang, Y.; Wang, H. An Evaluation Method for the Bursting Characteristics of Coal Under the Effect of Loading Rate. *Rock Mech. Rock Eng.* **2016**, *49*, 3281–3291. [[CrossRef](#)]
53. Zhang, Z.; Gao, F. Experimental investigations on energy evolution characteristics of coal, sandstone and granite during loading process. *Zhongguo Kuangye Daxue Xuebao J. China Univ. Min. Technol.* **2015**, *44*, 416–422.
54. Ma, S.; Zhou, H. Surface strain field evolution of rock specimen during failure process. *Yanshilixue Yu Gongcheng Xuebao Chin. J. Rock Mech. Eng.* **2008**, *27*, 1667–1673.
55. Yang, S.-Q.; Jing, H.-W.; Xu, T. Mechanical behavior and failure analysis of brittle sandstone specimens containing combined flaws under uniaxial compression. *J. Cent. South Univ.* **2014**, *21*, 2059–2073. [[CrossRef](#)]
56. Zhao, G.; Wang, E.; Wu, H.; Qiu, J.; Dai, Y. Micro-fracture evolution rule of sandstone specimens with a single hole under uniaxial compression. *Zhongnan Daxue Xuebao Ziran Kexue Ban J. Cent. South Univ. Sci. Technol.* **2019**, *50*, 1891–1900. [[CrossRef](#)]
57. Ma, W.; Chen, Y.; Yi, W.; Guo, S. Investigation on crack evolution behaviors and mechanism on rock-like specimen with two circular-holes under compression. *Theor. Appl. Fract. Mech.* **2022**, *118*, 103222. [[CrossRef](#)]
58. Reches, Z. Mechanisms of slip nucleation during earthquakes. *Earth Planet. Sci. Lett.* **1999**, *170*, 475–486. [[CrossRef](#)]
59. Xie, H.-P.; Ju, Y.; Li, L.-Y. Criteria for strength and structural failure of rocks based on energy dissipation and energy release principles. *Yanshilixue Yu Gongcheng Xuebao Chin. J. Rock Mech. Eng.* **2005**, *24*, 3003–3010.
60. Solecki, R.; Conant, R. *Advanced Mechanics of Materials*; Oxford University Press: Oxford, UK, 2003.
61. Li, X.B.; Lok, T.S.; Zhao, J. Dynamic characteristics of granite subjected to intermediate loading rate. *Rock Mech. Rock Eng.* **2005**, *38*, 21–39. [[CrossRef](#)]